

Specular interband Andreev reflections at van der Waals interfaces between graphene and NbSe₂

D. K. Efetov^{1*}, L. Wang², C. Handschin¹, K. B. Efetov^{3,4}, J. Shuang⁵, R. Cava⁵, T. Taniguchi⁶, K. Watanabe⁶, J. Hone², C. R. Dean¹ and P. Kim^{1*}

Electrons incident from a normal metal onto a superconductor are reflected back as holes—a process called Andreev reflection^{1–3}. In a normal metal where the Fermi energy is much larger than a typical superconducting gap, the reflected hole retraces the path taken by the incident electron. In graphene with low disorder, however, the Fermi energy can be tuned to be smaller than the superconducting gap. In this unusual limit, the holes are expected to be reflected specularly at the superconductor–graphene interface owing to the onset of interband Andreev processes, where the effective mass of the reflected holes changes sign^{4,5}. Here we present measurements of gate-modulated Andreev reflections across the low-disorder van der Waals interface formed between graphene and the superconducting NbSe₂. We find that the conductance across the graphene–superconductor interface exhibits a characteristic suppression when the Fermi energy is tuned to values smaller than the superconducting gap, a hallmark for the transition between intraband retro Andreev reflections and interband specular Andreev reflections.

Andreev reflection (AR) is a process transferring charges from a normal metal (N) into a superconductor (SC; refs 1–3). When an NS interface is biased with an energy eV_{ns} above the Fermi energy ε_{F} , an electron can only be injected into the SC gap Δ , if a hole is reflected back with an energy of eV_{ns} below ε_{F} , creating a Cooper pair at the Fermi level. For a straight N/SC interface, the momentum conservation along the boundary must be conserved. Thus the incidence angle of an incoming electron, θ_{inc} , and the reflected angle of a hole, θ_{ref} , have a simple relation $p_e \sin \theta_{\text{inc}} = p_h \sin \theta_{\text{ref}}$, where p_e and p_h are the total momentum of the electron and hole, respectively. In the limit $\varepsilon_{\text{F}} \gg \Delta$, which holds for a typical NS junction, the reflected hole is metal-like and remains in the conduction band of the normal metal, and therefore necessarily carries the opposite sign of the mass as compared to the electron. To conserve the momentum, the hole reflects back along a path of the incident electron, exhibiting nearly perfect retro-AR, with $\theta_{\text{ref}} \approx -\theta_{\text{inc}}$ (refs 6–8).

If, however, the Fermi energy can be tuned such that $\varepsilon_{\text{F}} \leq \Delta$, a completely different kind of AR is expected. In this case the energy difference, $2eV_{\text{ns}}$, provided by the AR process can result in the reflected hole appearing in the valence band rather than the conduction band. The reflected semiconductor-like hole now has the same mass sign as the incident electron, and therefore, according to momentum conservation, travels in the same direction along the interface ($\theta_{\text{ref}} > 0$ in Fig. 1). In the ultimate limit of $\varepsilon_{\text{F}} = 0$, the angle of reflection equals the angle of incidence $\theta_{\text{ref}} = \theta_{\text{inc}}$ —a process called specular reflection^{4,5}. The condition for specular-AR

is satisfied whenever $\Delta > eV_{\text{ns}} > \varepsilon_{\text{F}}$ (Fig. 1a right panel), and is therefore predicted to be observable when the normal metal in the N/SC junction consists of a zero-gap semiconductor (ZGS), and the Fermi energy is tuned close to the charge neutrality point (CNP) where the conduction band and valence band meet.

Graphene provides an ideal platform to exhibit both intraband and interband AR. Its two-dimensional nature and ZGS properties enable a crossover to be induced between intraband and interband AR by tuning ε_{F} through the electric field effect^{9–11}. However, accessing the regime $\varepsilon_{\text{F}} \sim \Delta$, a necessary condition to realize the interband AR, has been technically challenging. In typical graphene samples on a SiO₂ substrate, strong potential fluctuations up to $\delta\varepsilon_{\text{F}} \sim 50$ meV have been typically observed owing to the presence of charged impurities¹². This value is much larger than Δ in a typical SC. The recent progress in producing suspended¹³ and hexagonal boron nitride (hBN)-supported graphene samples¹⁴ has now allowed these fluctuations to be greatly reduced down to $\delta\varepsilon_{\text{F}} \sim 5$ meV (ref. 15). Despite the steady experimental progress that has been made in contacting graphene with various superconducting metals^{16–20}, including recent work on the edge contact on graphene^{21,22}, fabricating transparent SC contacts on graphene channels with extremely low inhomogeneity has yet to be realized.

In this letter we employ a novel non-invasive approach to fabricate N/SC interfaces with an unprecedented energy resolution close to the CNP. For this purpose we electronically couple (see Supplementary Information for details of the method) a high-mobility hBN/bilayer graphene (BLG) device and a 20–100 nm thin NbSe₂ flake. NbSe₂ is a van der Waals (vdW) SC with a critical temperature $T_c \sim 7$ K and a large $\Delta \sim 1.2$ meV (refs 23–25; Fig. 1b). We use the dry-vdW transfer technique and a current annealing method^{14,26} to achieve ohmic interfaces between graphene and NbSe₂ with a low junction resistance (see Supplementary Information). In this experiment, we chose BLG rather than single-layer graphene to minimize $\delta\varepsilon_{\text{F}}$ near the CNP. Owing to the larger density of states of BLG near the CNP, a smaller $\delta\varepsilon_{\text{F}}$ can be obtained in BLG given the similar level of substrate-induced inhomogeneity. The devices were fabricated on heavily degenerated Si substrates topped with 300 nm SiO₂, where a back-gate voltage V_{bg} is applied to tune the ε_{F} value of the BLG channel.

We characterize the electronic transport properties across the vdW N/SC junction by measuring the differential resistance dV/dI as a function of the channel current I_{sd} . The inset of Fig. 1c shows typical traces for a high back-gate voltage $V_{\text{bg}} = -50$ V that corresponds to a representative condition $\varepsilon_{\text{F}} \gg \Delta$.

¹Department of Physics, Columbia University, New York, New York 10027, USA. ²Department of Mechanical Engineering, Columbia University, New York, New York 10027, USA. ³Theoretische Physik III, Ruhr-Universität Bochum, D-44780 Bochum, Germany. ⁴National University of Science and Technology ‘MISIS’, Moscow 119049, Russia. ⁵Department of Chemistry, Princeton University, Princeton, New Jersey 08544, USA. ⁶National Institute for Materials Science, Namiki 1-1, Ibaraki 305-0044, Japan. *e-mail: defetov@mit.edu; pkim@physics.harvard.edu

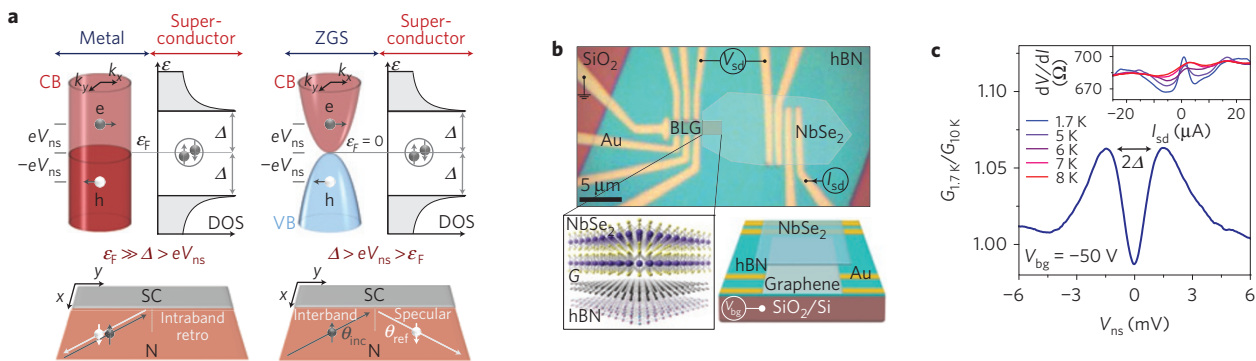


Figure 1 | Andreev reflections in hBN/BLG/NbSe₂ hetero-structures. **a**, Schematics of the AR processes at a normal metal/SC (left) and a zero-gap semiconductor/SC interface (right). An electron from the CB with a total energy of $\epsilon_F + eV_{ns}$ is reflected as a hole with an energy $\epsilon_F - eV_{ns}$, forming a Cooper pair at ϵ_F in the SC. For large ϵ_F the hole remains in the CB, resulting in an intraband retro-reflection process. For small enough ϵ_F the hole undergoes an interband transition into the VB, resulting in specular reflections. **b**, Top: colour-enhanced optical image of the hBN/BLG device before the transfer of the NbSe₂ flake (marking its final position). The NbSe₂ and the hBN/BLG stack form an electrically coupled overlap region. Bottom left: schematic diagram of the vertical cross-section of the vdW stack. Bottom right: sketch of the final device on top of a 300 nm SiO₂/Si back gate. **c**, Inset: temperature dependence of the differential resistance dV/dI versus bias current I_{sd} across the BLG/NbSe₂ interface at $V_{bg} = -50$ V. Strong variations of dV/dI appear below the NbSe₂ value of $T_c \sim 7$ K. Main: normalized conductance $G_{1.7K}/G_{10K}$ versus V_{ns} . The characteristic double-peak lineshape arises from ARs in the limit $\epsilon_F \gg \Delta$.

We observe that the $dV/dI(I_{sd})$ traces become increasingly nonlinear for temperatures $T < T_c$. To resolve these features better, we divide traces taken below and above T_c (here at $T = 1.7$ K and $T = 10$ K) and obtain the normalized differential conductance $G_{1.7K}/G_{10K} = (dV/dI_{10K}) / (dV/dI_{1.7K})$. Figure 1c shows $G_{1.7K}/G_{10K}$ as a function of the voltage drop across the N/SC junction V_{ns} , estimated by considering the BLG channel resistance (Supplementary Information). The most salient feature of the resulting $G_{1.7K}/G_{10K}(V_{ns})$ curve is a conductance dip around zero bias with two pronounced conductance peaks at $|V_{ns}| \sim \pm 1.2$ mV. The position of these peaks is consistent with the value of Δ_{NbSe_2} . Later, we will show that this lineshape is characteristic for typical N/SC junctions with $\epsilon_F \gg \Delta$ and can be explained in terms of intraband retro-ARs (refs 6–8,27).

The ability to tune ϵ_F enables us to investigate the characteristic AR signal at the continuous transition from large to small ϵ_F . The left panel of Fig. 2a shows the characteristic longitudinal resistance R_{xx} of the BLG channel versus V_{bg} . An upper bound of $\delta\epsilon_F < 1$ meV is estimated from the full-width at half-maximum (FWHM) of the $R_{xx}(V_{bg})$ peak^{13–15}, demonstrating that the condition $\epsilon_F < \Delta$ can be realized in this sample. The indirect estimates of $\delta\epsilon_F$ from the FWHM, however, are typically found to be much higher than from more direct measurements of $\delta\epsilon_F$ by scanning gate¹² or scanning tunnelling microscopy¹⁵, allowing one to assume a much smaller spatial energy variation in our sample. The right panel of Fig. 2a shows simultaneous measurements of $G_{1.7K}/G_{10K}$ as a function of both the voltage drop at the N/SC interface V_{ns} and V_{bg} . For large ϵ_F , $|V_{bg}| > 2$ V, $G_{1.7K}/G_{10K}(V_{ns})$ exhibits a similar behaviour to that described in Fig. 1c, showing the characteristic conductance dip around the zero-bias condition $V_{ns} = 0$. However, near the CNP, for $|V_{bg}| < 2$ V, the $G_{1.7K}/G_{10K}(V_{ns})$ traces exhibit marked variations. These result in dispersing conductance dip features that approximately follow the relation $|eV_{ns}| \sim |\epsilon_F|$ (Fig. 2c, top) and form a distinctive cross-like lineshape around the CNP point (Fig. 2a).

To explain these experimental findings at the crossover from the upper to the lower ϵ_F limit, we develop a theoretical model based on the Bogoliubov–de Gennes equations and the Blonder–Tinkham–Klapwijk (BTK) formalism for the conductance across the BLG/SC interface G_{ns} at $T = 0$ K. We also compute the normal conductance G_{nn} for $T > T_c$ (~ 10 K) (see Supplementary Information for details). Figure 2b shows the resulting normalized

conductance G_{ns}/G_{nn} as a function of ϵ_F and V_{ns} for energy ranges comparable to those in the experimental data. The theoretical model demonstrates qualitatively good agreement with the experimentally obtained normalized conductance in Fig. 2a. Conductance lineshapes in both regimes (Fig. 2c, bottom), the zero-bias conductance dips for $|\epsilon_F| \gg \Delta$ and the dispersing conductance dips for $|\epsilon_F| \sim \Delta$, are matched qualitatively and quantitatively with the theory. The slight asymmetry of the theoretical conductance around zero bias is due to the shift of the Fermi energy in the BLG channel when a bias voltage is applied across the N/SC junction.

Further quantitative comparison between the experiment and the theoretical model in the small-energy regime $|\epsilon_F| \sim \Delta$ can be performed by re-plotting the experimental $G_{1.7K}/G_{10K}$ map as a function of ϵ_F and V_{ns} (Fig. 3a—see Supplementary Information for the conversion scheme). In both graphs, one can identify four regions of enhanced conductance (coloured blue): two of them for $|\epsilon_F| > |eV_{ns}|$ and two for $|\epsilon_F| < |eV_{ns}|$. These regions are separated from each other by connected regions of reduced conductance (coloured red) that approximately follow the dependence $|\epsilon_F| \sim |eV_{ns}|$, forming diagonal lines that are roughly symmetrically arranged with respect to $\epsilon_F = eV_{ns} = 0$ in the conductance maps. Several representative line cuts, showing $G_{1.7K}/G_{10K}(\epsilon_F)$, clearly exhibit similar features for both experimental and theoretical traces, with good quantitative agreement for the positions of the conductance dips (Fig. 3b).

The various features observed in the conductance map can be explained by analysing the microscopic processes for different ϵ_F (Fig. 3c). ARs for SLG and BLG involve intervalley processes due to the time reversal symmetry of the backwards motion of the reflected hole^{4,16,17,28}. Therefore, for $\epsilon_F > eV_{ns}$, an electron in the K-valley of the CB with an energy of $\epsilon_F + eV_{ns}$ is reflected as a hole in the K'-valley of the CB with an energy $\epsilon_F - eV_{ns} > 0$. This intraband AR process gives rise to a relatively high conductance, analogous to ARs in normal metals in the limit $\epsilon_F \gg \Delta$. When ϵ_F decreases, however, the phase space for the reflected hole is decreased, resulting in a decreasing conductance. This effect culminates in a minimum in conductance at the condition $\epsilon_F = eV_{ns}$, where the hole is at the CNP and intraband ARs cease to exist. For $\epsilon_F < eV_{ns}$ the hole undergoes an interband transition into the VB and the conductance again increases.

This non-monotonic conductance change as a function of ϵ_F can be quantitatively explained by the existence of a critical angle

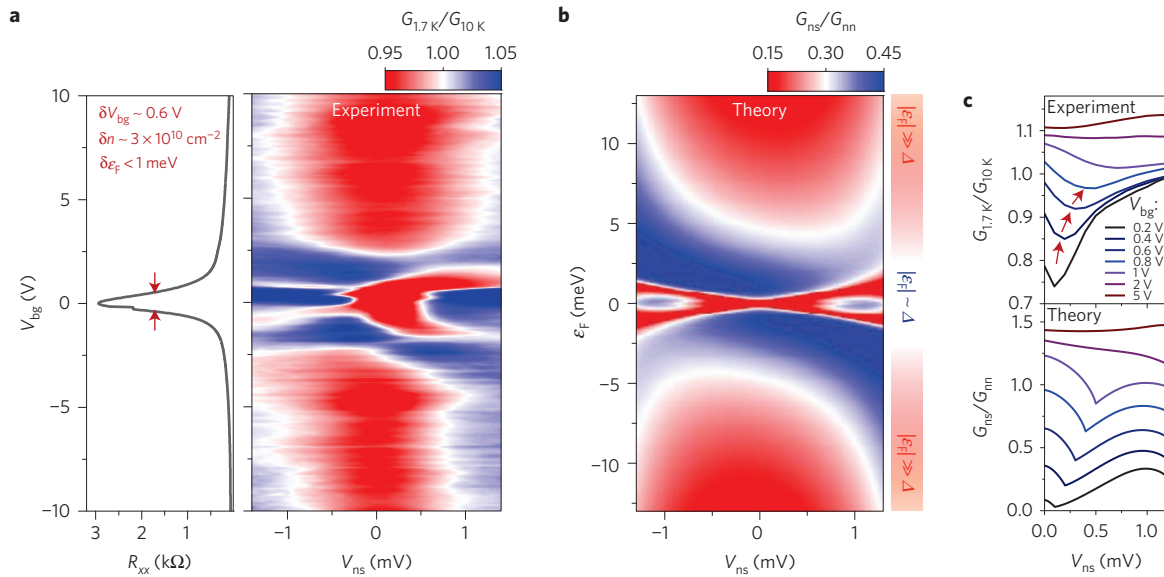


Figure 2 | Gate-tunable Andreev reflections. **a**, Left: R_{xx} versus V_{bg} , showing the characteristic channel resistance peak at the CNP with a FWHM of $\delta V_{bg} \sim 0.6$ V, suggesting an upper bound of $\delta \epsilon_F < 1$ meV. Right: colour map of the normalized differential conductance $G_{1.7K}/G_{10K}$ as a function of V_{ns} and V_{bg} for the inner gap region $|eV_{ns}| < \Delta$. **b**, Colour map of the theoretically obtained normalized differential conductance G_{ns}/G_{nn} versus V_{ns} and ϵ_F for the equivalent energy ranges used in the experimental data. The gate tunability of BLG allows the conductance changes to be probed continuously from the upper limit $|\epsilon_F| \gg \Delta$ to the lower limit $|\epsilon_F| \sim \Delta$. The zero-bias dip lineshape at large ϵ_F is continuously transformed into a diagonal cross-like lineshape close to the CNP. **c**, Curves of $G_{1.7K}/G_{10K}(V_{ns})$ (top) and $G_{ns}/G_{nn}(V_{ns})$ (bottom) for various fixed values of V_{bg} and the corresponding values of ϵ_F . Conductance dips for $eV_{ns} \sim \epsilon_F$ appear in the low-energy regime $|\epsilon_F| < \Delta$.

$\theta_c \equiv \sin^{-1} \sqrt{|\epsilon_F - eV_{ns}| / |\epsilon_F + eV_{ns}|}$ (Supplementary Information) that allows the AR process to happen only for electrons that are incident at $\theta_{inc} \leq \theta_c$. In the limit of the intraband AR ($\epsilon_F \gg eV_{ns}$) and the interband AR ($\epsilon_F \ll eV_{ns}$), $\theta_c \approx \pi/2$, and thus most electrons undergo AR processes resulting in a high conductance. However, for $\epsilon_F \sim eV_{ns}$, the critical angle approaches zero. If we assume a distribution of angles for the incident electrons, those outside of the critical angle will be reflected normally and only those arriving at near normal incidence will undergo AR processes, resulting in an overall suppressed conductance across the junction. For $\epsilon_F = eV_{ns}$, $\theta_c = 0$, and no electrons can enter the SC. The resulting conductance minima hence mark the exact crossover points between intraband and interband ARs.

We can now connect these processes with the corresponding changes in θ_{ref} (Fig. 3d,e). The dispersion relation $E(p_x, p_y)$ of BLG is shown in Fig. 3d, where p_x and p_y are momenta perpendicular and parallel to the N/SC interface, respectively. Considering that the parallel momentum p_y is conserved in the process⁴⁵, the excitation spectrum for ARs $\epsilon \equiv eV_{ns} = |E - \epsilon_F|$ can be expressed by a function of only p_x . Depending on the magnitude of the energy of the incident CB electron (assuming that it is in the K-valley) relative to ϵ_F , we can then relate the reflection process to three different scenarios: the first, with Andreev-reflected CB holes (normal AR); the second, in which all CB electrons are normally reflected (no AR); and the third, yielding Andreev-reflected VB holes (specular-AR), all in the K'-valley. For small $eV_{ns} \ll \epsilon_F$, p_x of the incident electron and the intraband reflected CB hole is almost unchanged. Because a CB hole has a negative mass, its negative p_x and the conserved p_y provide an overall direction of motion that retraces that of the incident electron (that is, the first scenario above). As V_{ns} grows, p_x of the reflected hole increases, translating into a larger θ_{ref} , that ultimately becomes $\pi/2$ when $\epsilon_F = eV_{ns}$ and $p_x = 0$. As V_{ns} grows further, so that $eV_{ns} > \epsilon_F$, the incident electron is reflected as an interband VB hole, which has a positive mass and a positive p_x that is opposite to the sign of p_x of the incident electron. Whereas the simultaneous sign changes of the mass and of p_x have no effect on the motion

in the x -direction, the sign change of the mass abruptly reverses the motion in the y -direction by 180° owing to the conservation of p_y , as described in the third scenario above. For the ultimate limits $\epsilon_F \gg \Delta$ and $\epsilon_F = 0$ one obtains perfect retro-reflections and specular reflections, respectively, with varying angles for intermediate energy scales and a discontinuous jump at $eV_{ns} = \epsilon_F$. Summarizing this discussion, the conductance maps in Fig. 3a can now be used as phase diagrams separating regions of retro-AR, where $|\epsilon_F| > |eV_{ns}|$, and specular-AR, where $|\epsilon_F| < |eV_{ns}|$.

Although our experimental findings are in good qualitative and quantitative agreement with the presented theory it is important to discuss possible deviations from it and rule out competing mechanisms. Most notably, the BLG band structure is renormalized when subjected to a transverse electric field and opens up a band gap¹¹. In our measurements an energy gap would manifest itself in a diamond-shaped region of suppressed conductance around zero energy, which is distinctly different from the observed cross-like shape that shows a dispersion following the relation $|eV_{ns}| \sim |\epsilon_F|$. Although we do observe a small region of reduced conductance around zero energy, the scale of these features is much smaller than the SC gap Δ . Indeed, we estimate the electric-field-induced gap for back-gated devices not to be bigger than 0.4 meV for an applied $V_{bg} = 0.75$ V (ref. 11; corresponding to $\epsilon_F = \Delta \sim 1.2$ meV). For such a small gap, interband transitions are still possible and specular-ARs can take place at slightly higher energies. Although additional deviations from the theory can also be attributed to imperfections due to a realistically broadened N/SC interface, inelastic scattering at finite temperatures, the presence of small potential fluctuations and a slightly renormalized BLG band structure¹¹, we can rule these out as key mechanisms for the observed features.

In conclusion our observation of gate-tunable transitions between retro- and specular-ARs opens a new route for future experiments that could employ the gate control of θ_{ref} , which can be continuously and independently altered with V_{bg} and V_{ns} . Most importantly, our findings help to draw a more general picture of the exact physical processes underlying ARs.

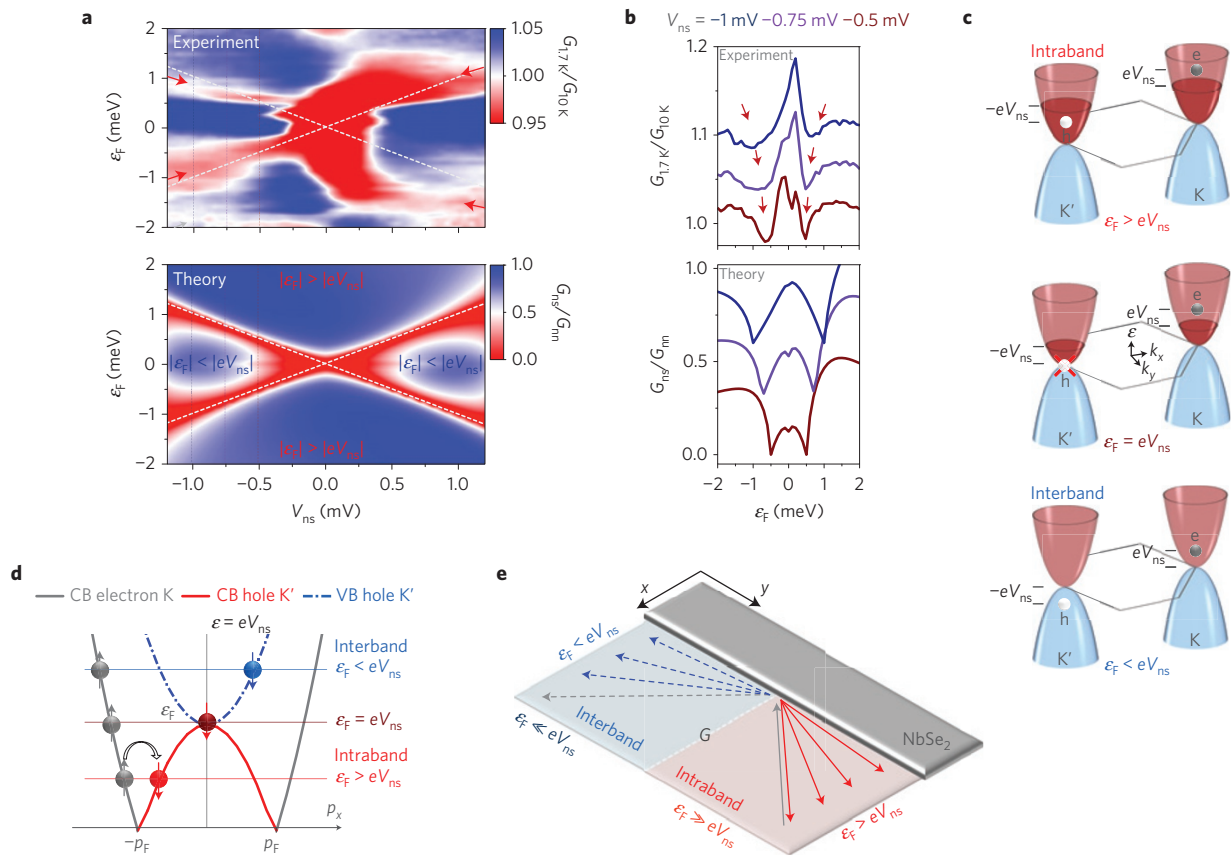


Figure 3 | Specular interband Andreev reflections at the CNP. **a**, Experimental $G_{1,7K}/G_{10K}$ and theoretical G_{ns}/G_{nn} colour maps as a function of V_{ns} and ϵ_F in the limit $|\epsilon_F| \sim \Delta$. A continuous region of lower conductance (red) that is defined for $|\epsilon_F| \sim |eV_{ns}|$ (white dashed lines) subdivides the map into four disconnected regions of comparatively high conductances (blue). In the regions where $|\epsilon_F| > |eV_{ns}|$ the ARs are of the retro type, whereas in the regions where $|\epsilon_F| < |eV_{ns}|$ the ARs are of the specular type. **b**, Experimental $G_{1,7K}/G_{10K}(\epsilon_F)$ and theoretical $G_{ns}/G_{nn}(\epsilon_F)$ line-traces demonstrate the evolution of the conductance dips (red arrows) with varying V_{ns} . **c**, Schematics of the AR process for BLG at the crossover from intradband to interband ARs. With decreasing ϵ_F at a fixed V_{ns} the AR hole moves from the CB to the VB. The crossover point where the hole is reflected onto the CNP is defined by $\epsilon_F = eV_{ns}$. **d**, Excitation spectrum $\epsilon(p_x) = eV_{ns}$ for a fixed $\epsilon_F < \Delta$. With an increasing excitation voltage V_{ns} , the momentum p_x of the reflected hole increases continuously from negative to positive values, passing through zero when $\epsilon_F = eV_{ns}$. Note that the quasi-particle excitation spectrum depends only on p_x , as p_y is conserved during the AR process. **e**, Schematics of the reflection angles of AR holes in the various energy limits. Starting from perfect intradband retro-reflections in the high- ϵ_F limit, θ_{ref} increases continuously towards $-\pi/2$ as ϵ_F is lowered. At the crossover point separating intradband and interband ARs, $\epsilon_F = eV_{ns}$, θ_{ref} exhibits a jump to $\pi/2$, which eventually results in perfect interband specular reflections ($\theta_{ref} = \theta_{inc}$) when $\epsilon_F = 0$.

Received 28 April 2015; accepted 5 November 2015; published online 7 December 2015

References

- Andreev, A. F. The thermal conductivity of the intermediate state in superconductors. *J. Exp. Theor. Phys.* **19**, 1228–1231 (1964).
- DeGennes, P. G. *Superconductivity of Metals and Alloys* (Benjamin, 1966).
- Tinkham, M. *Introduction to Superconductivity* (McGraw Hill, 1996).
- Beenakker, C. W. J. Specular Andreev reflection in graphene. *Phys. Rev. Lett.* **97**, 067007 (2006).
- Beenakker, C. W. J. Colloquium: Andreev reflection and Klein tunneling in graphene. *Rev. Mod. Phys.* **80**, 1337–1354 (2008).
- Klapwijk, T. M. Proximity effect from an Andreev perspective. *J. Supercond.* **17**, 593–611 (2004).
- Pannetier, B. & Courtois, H. Andreev reflection and proximity effect. *J. Low Temp. Phys.* **118**, 599–615 (2000).
- Blonder, G. E., Tinkham, M. & Klapwijk, T. M. Transition from metallic to tunneling regimes in superconducting microconstrictions: Excess current, charge imbalance, and supercurrent conversion. *Phys. Rev. B* **25**, 4515–4532 (1982).
- Das Sarma, S., Adam, S., Hwang, E. H. & Rossi, E. Electronic transport in two-dimensional graphene. *Rev. Mod. Phys.* **83**, 407–470 (2011).
- Wallace, P. R. The band theory of graphite. *Phys. Rev.* **71**, 622–634 (1947).
- McCann, E. & Fal'ko, V. Landau-level degeneracy and quantum Hall effect in a graphite bilayer. *Phys. Rev. Lett.* **96**, 086805 (2006).
- Martin, J. *et al.* Observation of electron–hole puddles in graphene using a scanning single-electron transistor. *Nature Phys.* **4**, 144–148 (2008).
- Bolotin, K., Sikes, K., Hone, J., Stormer, H. & Kim, P. Temperature-dependent transport in suspended graphene. *Phys. Rev. Lett.* **101**, 096802 (2008).
- Dean, C. R. *et al.* Boron nitride substrates for high-quality graphene electronics. *Nature Nanotech.* **5**, 722–726 (2010).
- Xue, J. M. *et al.* Scanning tunnelling microscopy and spectroscopy of ultra-flat graphene on hexagonal boron nitride. *Nature Mater.* **10**, 282–285 (2011).
- Heersche, H. B., Jarillo-Herrero, P., Oostinga, J. B., Vandersypen, L. M. K. & Morpurgo, A. F. Bipolar supercurrent in graphene. *Nature* **446**, 56–59 (2007).
- Du, X., Skachko, I. & Andrei, E. Y. Josephson current and multiple Andreev reflections in graphene SNS junctions. *Phys. Rev. B* **77**, 184507 (2008).
- Miao, F. *et al.* Phase-coherent transport in graphene quantum billiards. *Science* **317**, 1530–1533 (2007).
- Popinciuc, M. *et al.* Zero-bias conductance peak and Josephson effect in graphene-NbTiN junctions. *Phys. Rev. B* **85**, 205404 (2012).
- Rickhaus, P., Weiss, M., Marot, L. & Schonenberger, C. Quantum Hall effect in graphene with superconducting electrodes. *Nano Lett.* **12**, 1942–1945 (2012).
- Calado, V. E. *et al.* Ballistic Josephson junctions in edge-contacted graphene. *Nature Nanotech.* **10**, 761–764 (2015).
- Ben Shalom, M. *et al.* Proximity superconductivity in ballistic graphene, from Fabry–Perot oscillations to random Andreev states in magnetic field. Preprint at <http://arXiv.org/abs/1504.03286> (2015).
- Clayman, B. P. & Frindt, R. F. Superconducting energy gap of NbSe₂. *Solid State Commun.* **9**, 1881–1884 (1971).

24. Frindt, R. F. Superconductivity in ultrathin NbSe₂ layers. *Phys. Rev. Lett.* **28**, 299–301 (1972).
25. Staley, N. E. *et al.* Electric field effect on superconductivity in atomically thin flakes of NbSe₂. *Phys. Rev. B* **80**, 184505 (2009).
26. Geim, A. K. & Grigorieva, I. V. Van der Waals heterostructures. *Nature* **499**, 419–425 (2013).
27. Efetov, D. K. *Towards Inducing Superconductivity into Graphene* PhD thesis, Univ. Columbia (2014).
28. Ludwig, T. Andreev reflection in bilayer graphene. *Phys. Rev. B* **75**, 195322 (2007).

Acknowledgements

The authors gratefully acknowledge fruitful discussions with C. Beenakker, I. Aleiner, L. Levitov, A. McDonald, A. Volkov, P. Jarrillo-Herrero, A. Akhmerov, C. Schoenenberger, M. Devoret and J. Pillet. D.K.E. acknowledges the support of the FAME Center, sponsored by SRC MARCO and DARPA. P.K. acknowledge support by DOE (DE-FG02-05ER46215) and C.H. is supported by AFOSR (FA2386-13-1-4122). K.B.E. gratefully acknowledges the financial support of the Ministry of Education and Science of the Russian Federation in the framework of Increase Competitiveness Program of NUST 'MISI' (Nr. K2-2014-015) as well as of Transregio 12 and Priority

Program 1459 'Graphene' of *Deutsche Forschungsgemeinschaft*. K.W. and T.T. acknowledge support from the Elemental Strategy Initiative conducted by the MEXT, Japan. T.T. acknowledges support from a Grant-in-Aid for Scientific Research on Grant 262480621 and on Innovative Areas Nano Informatics (Grant 25106006) from JSPS. J.H. acknowledges the NSF DMR-1122594 grant.

Author contributions

D.K.E. and P.K. conceived the experiment. D.K.E. carried out the electrical measurements. D.K.E., L.W. and C.H. fabricated the devices. J.S. and R.C. grew the NbSe₂ crystals. T.T. and K.W. grew the hBN crystals. D.K.E. and P.K. performed data analysis. D.K.E. and K.B.E. developed the theoretical model. C.R.D., J.H. and P.K. supervised the experiments. All authors discussed the results and D.K.E. and P.K. wrote the manuscript.

Additional information

Supplementary information is available in the [online version of the paper](#). Reprints and permissions information is available online at www.nature.com/reprints. Correspondence and requests for materials should be addressed to D.K.E. or P.K.

Competing financial interests

The authors declare no competing financial interests.